RSC Advances

PAPER

View Article Online
View Journal | View Issue

Cite this: *RSC Adv.*, 2017, **7**, 51359

Sawdust as an effective biotemplate for the synthesis of $Ce_{0.8}Zr_{0.2}O_2$ and $CuO–Ce_{0.8}Zr_{0.2}O_2$ catalysts for total CO oxidation†

Igor Yu. Kaplin,* Ekaterina S. Lokteva, Elena V. Golubina, Konstantin I. Maslakov, Natalia E. Strokova, Sergei A. Chernyak and Valery V. Lunin

Wood sawdust (SD) was successfully used as a biotemplate to prepare precursors of $Ce_{0.8}Zr_{0.2}O_2$ (CZ) and $CuO–Ce_{0.8}Zr_{0.2}O_2$ (Cu–CZ, about 25% of CuO) catalysts, which were tested in total CO oxidation at 100–400 °C after calcination at 500 or 600 °C, and compared with analogous systems prepared using cetyltrimethylammonium bromide (CTAB). The improved specific surface area and oxygen mobility of the catalysts calcined at 500 °C resulted in an increased efficiency in CO oxidation. CZ (SD-500) demonstrated much higher catalytic efficiency than the CZ (CTAB-500) sample despite having a two times less S_{BET} due to the promoting action of Ca and K inherited from sawdust and improved concentration of superoxide surface centers. Both facilitation of CO adsorption on peroxide and superoxide centers and increased oxygen mobility provide improvement in the high-temperature efficiency of biomorphic CZ in CO oxidation. The XRD, XPS and TPR data testify that Cu in modified systems partially exists as a separate CuO phase, in small amounts as Cu^+, and partially is incorporated in the surface $Cu_yCe_xZr_{1-x-y}O_{2-z}$ and/or $Cu_yCe_{1-y}O_{2-x}$ phases. Modification with Cu enhances the low-temperature efficiency of CZ systems, prepared using both templates and calcined at 500 °C. Cu–CZ (SD-500) was a bit less active than Cu–CZ (CTAB-500) only at 100–150 °C, primarily due to the decreased CuO content, and the difference in CuO interaction with CZ support, found by TPR. Presumably CuO provides low-temperature CO oxidation through the Langmuir–Hinshelwood mechanism; the Cu^+/Cu^{2+} pair can also participate as an additional redox pair in high-temperature CO oxidation by the Mars–van-Krevelen mechanism.

Received 29th September 2017
Accepted 19th October 2017

DOI: 10.1039/c7ra10791a

rsc.li/rsc-advances

1. Introduction

It is widely known that the efficiency of catalytic systems can be tuned by modification of the preparation technique. Biotemplate methods have attracted considerable interest in the past decades.[1] Natural biological materials such as rattan, rice husk, cellulose, paper[2–5] and widespread wood substances[6,7] are used as a template for the synthesis of promising biomorphic ceramic materials of various chemical composition and texture for diverse applications. Biotemplating is an especially suitable method of mixed oxide preparation as it helps to avoid the segregation of individual components of multi-component oxides.[5] The use of natural templates, especially waste materials such as wood sawdust, complies with the principles of green chemistry. Moreover, biotemplates impart to the biomorphic oxide materials the unique textural properties of natural ones, which is very promising for catalytic applications. Furthermore, minor components of biotemplates, *e.g.* ash admixtures, could serve as catalyst promoters. Little attention has been paid in the literature to this aspect of biotemplating.

Due to their unique redox properties Ce-containing oxides are among the most important component of three-way catalysts (TWCs) which transform CO, NO_x and hydrocarbons to harmless CO_2, N_2 and water.[8] Easy electron transfer between Ce^{4+} and Ce^{3+} ions provides increased mobility of the lattice oxygen, which can be donated or accepted by oxide depending on the reaction conditions.[9]

The incorporation of Zr^{4+} into the CeO_2 lattice to form mixed $Ce_{1-x}Zr_xO_2$ oxides increases thermal stability and allows the formation of a highly defective structure,[10,11] which additionally improves bulk mobility of the lattice oxygen.[12] This mobility is known to be a necessary condition of fast redox processes on the oxide surface.

There is some evidence in literature that the addition of CaO[13–17] and alkali metals[13,18] influences the catalytic properties of ceria and CZ systems. At the same time, they are among the main ash impurities in wood materials.[19] Therefore, we can expect additional improvement of the catalytic action of biomorphic CZ produced using wood as a template.

Lomonosov Moscow State University, Chemistry Department, Leninskie Gory 1/3, Moscow, 119991, Russia. E-mail: kaplinigormsu@gmail.com

† Electronic supplementary information (ESI) available. See DOI: 10.1039/c7ra10791a

Modification of CeO_2 or $Ce_{1-x}Zr_xO_2$ with CuO results in a synergy in CO oxidation.[20,21] Simultaneous participation of two redox pairs (Cu^{2+}/Cu^{1+} and Ce^{4+}/Ce^{3+}) in a catalytic cycle was proposed to be a reason for positive Cu influence.[22] The activity of CuO–CeO_2 catalysts in CO oxidation shows a strong dependence on the preparation method,[23] but to the best of our knowledge the catalytic properties of Cu–CZ prepared using wood as a biotemplate have not been studied earlier.

The present paper focuses on filling this gap in the case of ceria–zirconia double oxides, both pristine and modified with CuO. For this purpose, double $Ce_{0.8}Zr_{0.2}O_2$ and triple CuO–$Ce_{0.8}Zr_{0.2}O_2$ oxide systems were prepared using pine sawdust as a biotemplate. The influence of the calcination temperature of these systems and their modification with CuO additive on the physicochemical properties is discussed. Catalytic properties were tested in CO oxidation in a stoichiometric CO : O_2 mixture. Catalysts of the same composition but prepared using the organic surfactant cetyltrimethylammonium bromide (CTAB) as a template were used as comparative samples.

2. Experimental

2.1. Catalyst preparation

The cerium to zirconium ratio in the catalysts (4 : 1) was chosen based on our previous work.[24] Biomorphic Ce–Zr oxide with a Ce : Zr molar ratio of 4 : 1 showed better efficiency in CO oxidation in comparison with higher Zr loaded oxide systems.

$Ce_{0.8}Zr_{0.2}O_2$ and CuO–$Ce_{0.8}Zr_{0.2}O_2$ biomorphic systems were prepared by the impregnation of ~15 g of pine (*Pinus sylvestris*) sawdust (SD, sieved fraction 0.25–0.5 mm) with the solutions of calculated amounts of metal salts $ZrO(NO_3)_2 \cdot H_2O$ (99.5%, Acros Organics), $(NH_4)_2[Ce(NO_3)_6]$ (chemically pure, Reachim), and $Cu(CH_3COO)_2 \cdot H_2O$ (analytically pure, Vecton) for the CuO modified samples.

Impregnated sawdust was dried for 3–4 h at 120 °C to produce catalyst precursors, denoted as CZ (SD) and Cu–CZ (SD). Then the precursors were calcined at 500 °C for 3.5 h or at 600 °C for 4 h. These samples were named CZ (SD-500), Cu–CZ (SD-500), CZ (SD-600), and Cu–CZ (SD-600).

The intended molar ratio was Ce : Zr = 4 : 1 for CZ and Cu : Ce : Zr = 1.67 : 4 : 1 (25 mol% Cu) for Cu–CZ. The total amount of metal salts was 0.01 mol in each case.

The comparative oxide systems were produced by a surfactant-assisted method using cetyltrimethylammonium bromide (CTAB) as a template.[25] Water solutions of calculated amounts of $ZrO(NO_3)_2 \cdot H_2O$, $(NH_4)_2[Ce(NO_3)_6]$ and $Cu(CH_3COO)_2 \cdot H_2O$ for the CuO modified samples and of 0.005 mol citric acid monohydrate ($C_6H_8O_7 \cdot H_2O$) (pure, Reachem) were simultaneously and slowly added to an ethanol solution of 0.005 mol CTAB (99%, BioChemica) with further continuous stirring for 1 h and evaporation of the solvents to form a gel-like substance. The gel was dried for 3 h at 120 °C to form a precursor of the catalysts. The precursor was calcined at 500 °C for 3.5 h or at 600 °C for 4 h to form CZ (CTAB-500), Cu–CZ (CTAB-500), CZ (CTAB-600), and Cu–CZ (CTAB-600). Sample designations are summarized in Table 1.

2.2. Characterization

Scanning electron microscopy combined with energy dispersive X-ray spectroscopy (SEM/EDS) was performed on a JSM-6390LA (JEOL Ltd., Japan) instrument equipped with an EDS unit.

The diffraction patterns were obtained using Bruker D8 Advance (Germany) and Rigaku MiniFlex 300/600 (Japan) powder diffractometers (CuKα radiation, 1.5418 Å). The XRD patterns were collected in a 2θ range of 10–70° with a step size of 0.02°. The JCPDS-PDF2 ICDD (International Center for Diffraction Data) library was used for the identification of phases.

The lattice parameters were calculated using the equation: $a = d_{hkl}\sqrt{h^2 + k^2 + l^2}$, where d_{hkl} is the interplanar distance, and h, k, and l are Miller indices of crystallographic planes.

The average size of the crystallites was estimated using the Scherrer equation[26] for the most intense reflection peaks:

$$D = \frac{0.9\lambda}{\Delta(2\theta)\cos\theta},$$

where D is the size of the coherent scattering region, $\Delta(2\theta)$ is the half-width of the reflex in the diffraction pattern, λ is the X-ray wavelength, and θ is the diffraction angle. The mean size of the CuO crystallites was estimated using reflexes at 2θ = 35.5 and 38.7°.

The XPS spectra were acquired on an Axis Ultra DLD spectrometer (Kratos Analytical, UK) using a monochromatic AlK* source ($h\nu$ = 1486.7 eV, 150 W). The pass energy of the analyser was 40 eV. The binding energy (EB) scale of the spectrometer was preliminarily calibrated using the position of the peaks for the Au $4f_{7/2}$ (83.96 eV) and Cu $2p_{3/2}$ (932.62 eV) core levels of pure metallic gold and copper. The powder samples were mounted on a holder using double-sided adhesive tape. The Kratos charge neutraliser system was used, and the spectra were charge-corrected to give a Zr $3d_{5/2}$ peak at a binding energy of 182.1 eV typical for Zr^{4+} ions.

The BET specific surface area (S_{BET}) was determined by low temperature N_2 adsorption using an Autosorb-1 (Quantachrome, USA) physisorption analyzer. Samples were preliminarily degassed at 200 °C for 3 h.

Temperature-programmed reduction (TPR) was performed on a USGA-101 (UNISIT, Russia) chemisorption analyzer. Pure NiO was used for the preliminary calibration of the instrument. In a typical experiment, approx. 0.050 g of the sample was heated at 300 °C under Ar flow for 0.5 h, cooled down to 30 °C and heated again under diluted hydrogen flow (30 mL min^{-1}, 5% H_2 in Ar) from 30 to 850 °C at a 10 °C min^{-1} heating rate.

Thermal analysis was performed using an STA 449C (Jupiter, NETZSCH, Germany) synchronous thermal analyzer under air flow with a heating rate of 5 °C min^{-1}. The samples produced using CTAB and SD were heated from room temperature to 800 °C or 1000 °C, respectively, at a 35 mL min^{-1} flow rate. The heat effects (DSC) and thermogravimetric curve (TG) were recorded simultaneously.

Cu content in the samples was measured by atomic absorption spectroscopy (AAS) on a Thermo Fisher Scientific series iCE 3000 spectrophotometer (USA) using atomization in an air–acetylene flame. Device control and processing of the

Table 1 CuO content and S_{BET}, XRD, XPS and SEM-EDS results for the studied samples

Sample	CuO content[a] (mol%)	S_{BET}[b] ($m^2\ g^{-1}$)	Lattice parameter a[c] (Å)	CuO crystallite size[c] (nm)	XPS results			Surface content found by SEM-EDS, at%	
					Ce^{3+}/Ce^{4+}	Cu^{+}/Cu^{2+}	O_{act} (%)	Ca	K
CZ (CTAB-500)	—	165 ± 17	5.425 ± 0.002	—	0.19	—	15.5	—	—
CZ (CTAB-600)	—	75 ± 8	5.398 ± 0.005	—	0.11	—	13.9	—	—
Cu–CZ (CTAB-500)	29.0	89 ± 9	5.400 ± 0.001	13.0 ± 0.5	0.00	0.23	17.7	—	—
Cu–CZ (CTAB-600)	21.2	62 ± 6	5.399 ± 0.009	13.8 ± 0.6	0.05	1.70	15.3	—	—
CZ (SD-500)	—	45 ± 5	5.419 ± 0.002	—	0.14	—	17.1	1.2	0.4
CZ (SD-600)	—	35 ± 4	5.409 ± 0.004	—	0.09	—	15.1	1.4	0.3
Cu–CZ (SD-500)	22.6	93 ± 9	5.394 ± 0.002	12.0 ± 0.3	0.02	0.25	22.1	1.1	—
Cu–CZ (SD-600)	21.7	37 ± 4	5.413 ± 0.003	12.3 ± 0.5	0.01	1.33	15.8	2.3	0.4

[a] Found by AAS. [b] S_{BET} – the specific surface area determined by the multi-point BET method. [c] On the basis of XRD data.

results were performed using SOLAAR Data Station software. Before analysis, solid samples were dissolved by heating in a mixture of $(NH_4)_2SO_4$ and concentrated H_2SO_4 (1 : 2 molar ratio).

The solution was then diluted with distilled water up to a desired volume. Standard solutions for calibration curves were prepared taking into account the background concentrations of Ce and Zr in the tested solutions.

2.3. Catalytic tests

The samples were tested in total CO oxidation using a fixed-bed pulse microcatalytic set. A weighed amount of catalyst (0.1 g) was placed in a quartz flow reactor equipped with a thermocouple and a tubular furnace. The desired temperature of the reaction was adjusted at a constant flow of He (60 mL min^{-1}) through the reactor. Pulses of the reaction mixture (2 vol% CO and 1 vol% O_2 in He) were fed into the reactor using a 6-way valve with a calibrated gas loop (1 mL). The products were analyzed by online gas chromatography (GC) using a thermal conductivity detector and 1 m packed column (Porapak Q). The stationary conversion in the isothermal mode used to plot the kinetics curves was achieved after 10–12 pulses and remained constant for at least 10 pulses.

The fraction of CO_2 formed (X_{CO_2}) was determined using the following equation:

$$X_{CO_2} = \frac{S_{CO_2}}{S_{CO} + S_{CO_2}},$$

where S_{CO} and S_{CO_2} are the areas of chromatographic peaks of CO and CO_2, respectively.

3. Results and discussion

3.1. Physical and textural properties

3.1.1. The choice of calcination conditions. To select the calcination temperature appropriate for the complete removal of the template from the catalyst precursor, its thermal decomposition and phase transitions were analyzed by DSC-TG. Non-modified CZ (SD) and CZ (CTAB) systems were studied in our recent work.[24] The most intense mass loss was observed at 220–280 °C for CZ (CTAB) and at 225–425 °C for CZ (SD).

The DSC-TG curves of Cu–CZ (SD) and Cu–CZ (CTAB) are presented in Fig. 1. The small mass loss at 50–200 °C accompanied by endothermic peaks at 90 and 190 °C in the DSC curve of Cu–CZ (SD) (Fig. 1a) results from the evaporation of physically bound absorbed water.[27] The significant mass loss in the temperature range of 225–425 °C accompanied by a broad and intense exothermic peak with a maximum at about 345–400 °C corresponds to the decomposition of main wood components: cellulose, hemicellulose and lignin. Most likely the decomposition of the metal salts used as metal precursors also takes place in this temperature range. Separate exothermic peaks of the decomposition of each metal salt overlap with the broad peak of heat evolution in the range of 225–425 °C and therefore are not visible in DSC curves. Since no mass changes or thermal effects are observed at temperatures above 425 °C, the decomposition processes are accomplished below this point, and no phase transformations occur at higher temperatures.

The DSC and TG curves of the Cu–CZ (CTAB) precursor are shown in Fig. 1b. The endothermic peak in the DSC curve in the temperature range of 80–100 °C and the corresponding mass loss (3.3%) result from water desorption. CTAB burning out produces a narrow intense peak of heat evolution with a maximum at 260 °C.[21,25] The less intense exothermic peak at 218 °C probably arises due to the start of $Cu(CH_3COO)_2$ and citric acid decomposition. The mass loss and heat release peaks at 308 °C could also be caused by salt decomposition. In ref. 28 thermal decomposition of freeze-dried copper(II) acetate monohydrate was investigated by DSC-TG to propose a set of reactions defining the composition of the final product. It was found that calcination at 325–425 °C resulted in the formation of several coexisting phases that were identified by XRD and HT XRD as Cu^0, Cu_2O and CuO, but the final product formed above 525 °C was CuO. $ZrO(NO_3)_2 \cdot H_2O$ used in our work as a Zr source undergoes dehydration at 85–180 °C and decomposition at 180–350 °C accompanied with gaseous NO_x evolution[29] that proceeds in a similar temperature range of 180–280 °C.[30] No mass changes or thermal effects and therefore no phase

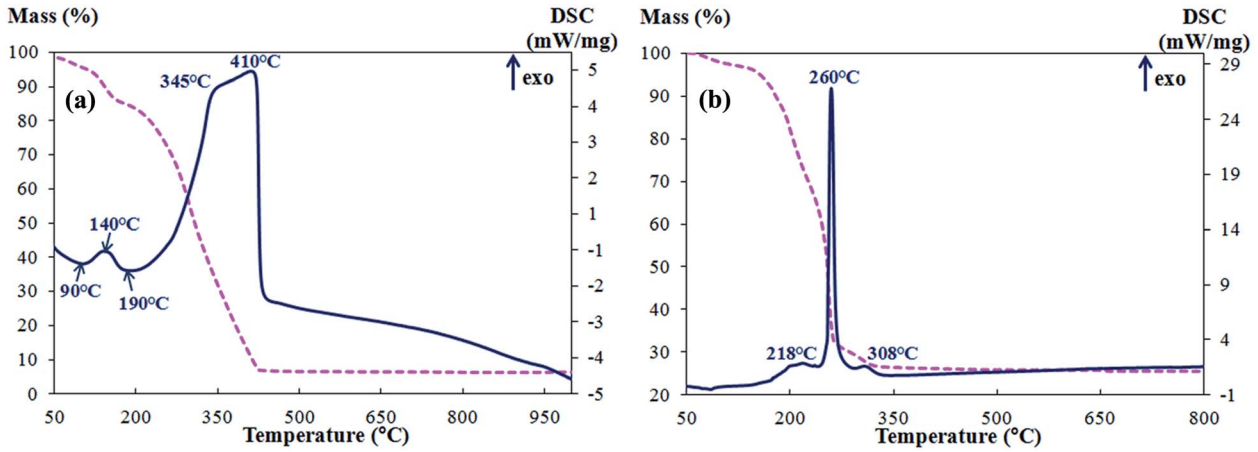

Fig. 1 DSC-TG profiles of Cu–CZ (SD) (a) and Cu–CZ (CTAB) (b) precursors of Cu-containing catalysts.

transformations were observed during further heating above 325 °C. Thus, calcination at a temperature of 325 °C is effective for the formation and crystallization of CZ and CuO from the corresponding salts.

The comparison of the DSC-TG data for the Cu–CZ (SD) and Cu–CZ (CTAB) samples reveals the difference in template removal: the organic CTAB template burns out in a narrow temperature range, whereas sawdust removal takes place in a significantly wider temperature range. This fact is consistent with the chemical nature of the templates: CTAB is an individual chemical compound whereas wood substance comprises a set of organic fragments of various compositions.

Based on the DSC-TG data for the catalyst precursors, two different temperatures of 500 and 600 °C were chosen for calcination. Incomplete sawdust decomposition is possible at temperatures below 500 °C whereas temperatures higher than 600 °C can cause excessive crystal growth and a decrease in S_{BET}, and eventually deterioration of the catalytic efficiency of the calcined material. Such a trend was earlier observed for a CuO/$Ce_{0.8}Zr_{0.2}O_2$ system prepared by a surfactant-assisted method.[21]

3.1.2. Texture analysis by SEM and N_2 physisorption. The surface texture of the samples was investigated by SEM and low-temperature N_2 sorption. The SEM images of the double CZ systems prepared using CTAB and SD are similar to those presented in ref. 24. Their comparison with the micrographs of the Cu-modified samples presented in Fig. 2 demonstrates that copper modification does not affect the texture of CZ. Particle aggregates of the CTAB-templated systems show an irregular shape and broad size distribution of about 10 μm or even more. The size of the large pores visible in the SEM images is less than 10 or even 5 μm. The number of large pores visible in the SEM images is low, but the possibility of the presence of submicron and nanometer-sized pores (less than 50 nm) could not be excluded. The change in calcination temperature has no influence on the micron level texture characteristics of the CTAB-templated samples.

The surface texture of the biomorphic systems is drastically different: it reproduces the fibrous texture of wood sawdust used as a template.[24] Like the CZ (CTAB) samples, the texture of the biomorphic samples does not depend on the calcination temperature.

Elemental composition of the samples was determined by EDS during SEM investigation. It was found that the surface of the CTAB-templated oxides, in addition to Ce, Zr and O, contains C and Br residues of the decomposition of CTAB and citric acid (the carbon content on the surface of all samples was between 15 and 20 at% and the Br content was between 0.5 to 1.5 at%). A similar amount of residual carbon after sawdust burning was found on the surface of the biomorphic oxides as well. These samples also contain small amounts of Ca and K (Table 1) inherited from raw sawdust. The presence of such impurities can enhance the catalytic efficiency. These elements are known to serve as promoters for Ce-containing catalysts of soot and CO oxidation.[13,18]

EDS element maps demonstrate the uniform distribution of Ce and Zr on the surface of all samples (see Fig. S1a and b in the ESI†), possibly due to the presence of a single phase containing both elements.

The content of copper in the modified samples was measured by AAS (Table 1). The CuO loading was 29 mol% in Cu–CZ (CTAB-500) and about 20–23 mol% in the other three samples. The difference can be explained by the separate preparation of the precursor for each sample.

The BET specific surface area of the samples is presented in Table 1. Both the increase of calcination temperature and modification with CuO lead to a decrease of S_{BET} of the CTAB-templated samples possibly due to sintering and blocking of the pore openings with CuO agglomerates. The same trends were observed in other studies.[21,31]

The biomorphic systems demonstrate lower S_{BET} than the CTAB-templated ones. It seems that the biotemplate promotes the development of macroporosity which was confirmed by SEM, but it is less effective in the micro- and mesopore formation than CTAB. In contrast with the CTAB-templated oxides, Cu modification has nearly no influence on the S_{BET} of the biomorphic samples calcined at 600 °C, and significantly improves the S_{BET} of the modified Cu–CZ (SD-500) sample in comparison with non-modified CZ (SD-500). Thus, the S_{BET}

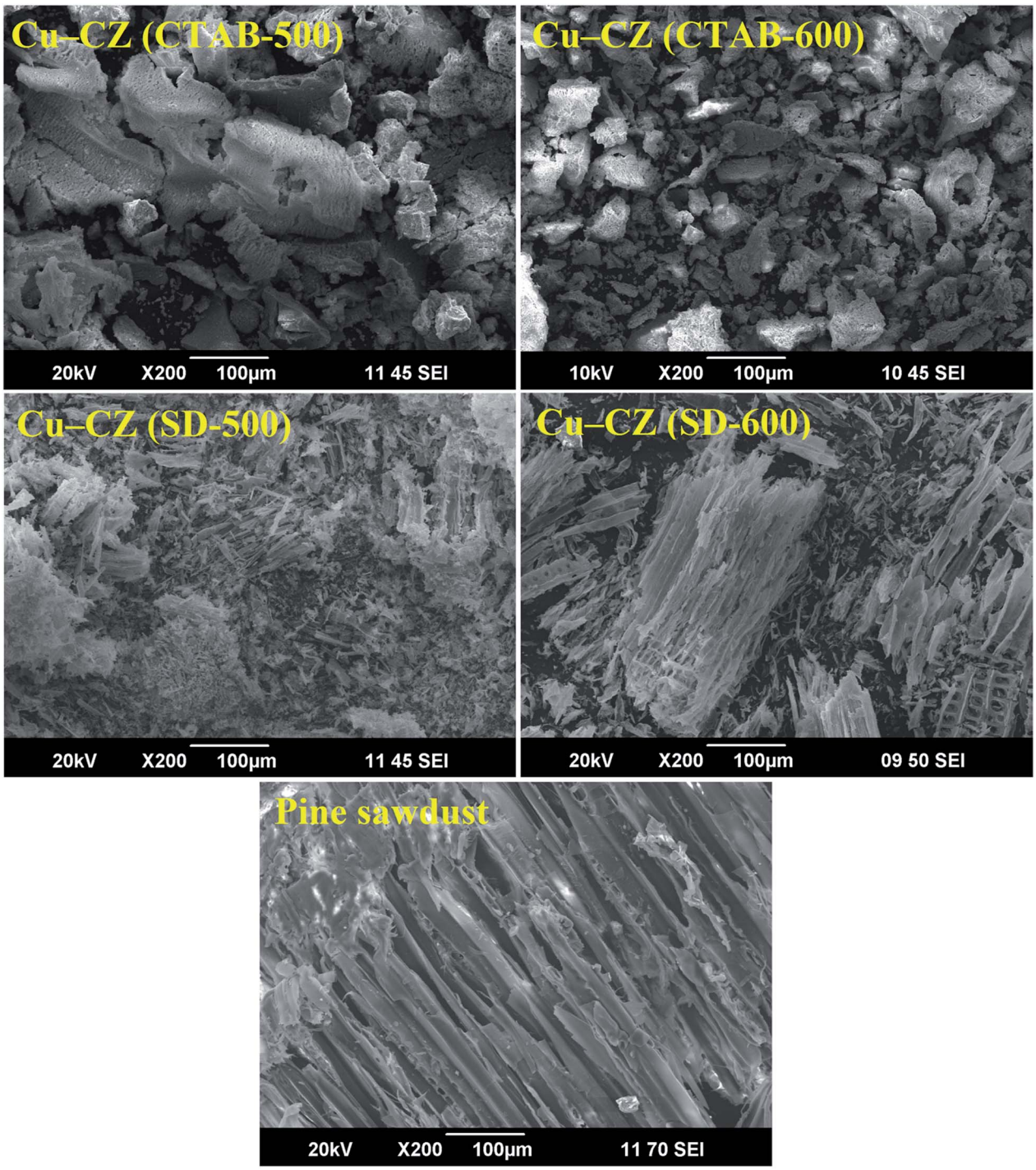

Fig. 2 SEM images of Cu–CZ (CTAB-500), Cu–CZ (CTAB-600), Cu–CZ (SD-500), Cu–CZ (SD-600) and pine sawdust.

values of Cu–CZ (SD-500) and Cu–CZ (CTAB-500) are comparable.

Both SEM and N_2 adsorption methods reveal that the texture of the samples depends strongly on the template used, and this difference could influence the catalytic properties in CO oxidation. The presence of mesopores[32] or meso–macropores[31,33] in oxide catalysts usually provides high catalytic efficiency in CO oxidation. The presence of ash impurities as minor components distinguishes the biomorphic samples from the CTAB-templated ones.

3.1.3. XRD study. XRD patterns of the SD- and CTAB-templated samples are presented in Fig. 3. The main reflexes of CeO_2 (JSPDS no. 34-0394, space group $Fm\bar{3}m$) and tetragonal ZrO_2 (JSPDS no. 01-073-1441, space group $P4_2/nmc$) are shown in Fig. 3 for comparison.

There is no significant difference in the XRD patterns of the samples prepared using the SD and CTAB templates. All of them show symmetric reflexes at $2\theta = 28.79$, 33.36, 47.90, and 56.85° corresponding to CZ with Ce : Zr $\approx$ 4 crystallized in a cubic

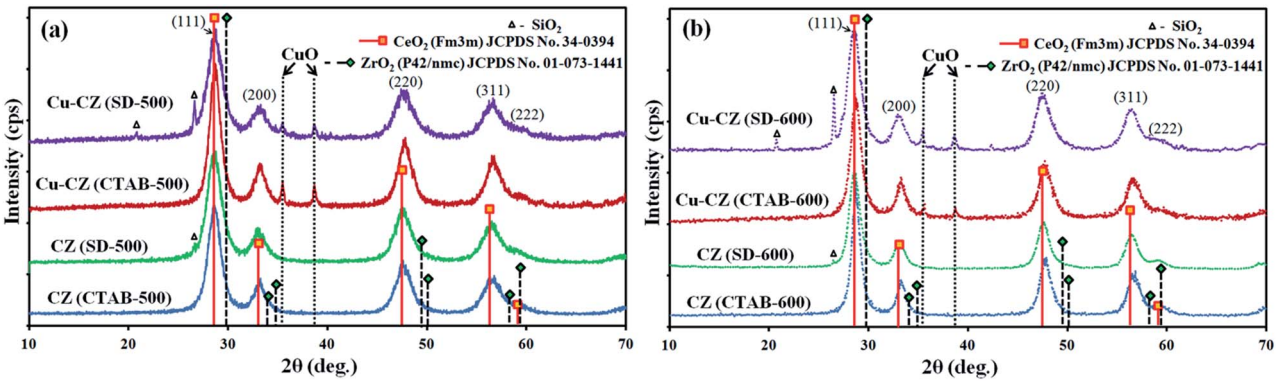

Fig. 3 XRD patterns of SD- and CTAB-templated samples calcined at 500 °C (a) and 600 °C (b).

phase of fluorite structural type.[21] The presence of CZ mixed oxide in all samples agrees with the SEM-EDS results which testifies the uniform distribution of Ce and Zr.

Diffraction patterns of the Cu-containing samples comprise weak reflexes at 2θ of 35.5 and 38.7°, which can be attributed to a separate CuO phase (tenorite, space group $B2/b$).

The significant width of the CZ mixed oxide reflexes in the diffraction patterns of all samples can be caused by the presence of a small amount of tetragonal CZ phase,[34] or, more probably, by the small size of coherent scattering regions. Their size was estimated on the basis of the Scherrer equation (see Subsection 2.2.). A known trend of crystallinity improvement when raising the calcination temperature is observed in our case as a moderate increase of CZ crystal size with the increase of calcination temperature from 500 to 600 °C. No influence of the calcination temperature on the size of the CuO crystals was observed. The comparison of the average size of the CuO crystals (13–13.8 nm, see Table 1) and the average pore size for the Cu–CZ (CTAB) samples (pore width of about 3.6 nm) confirms the possibility of pore blocking by CuO.

The cell parameter a was calculated from the XRD data as well (Table 1). Modification by CuO leads to a visible decrease of the parameter both for the CTAB and SD samples calcined at 500 °C in comparison with those calcined at 600 °C, possibly due to the presence of minor amounts of triple oxide Cu_yCe_x-$Zr_{1-x-y}O_{2-z}$ and/or double oxide $Cu_yCe_{1-y}O_{2-x}$.[35,36]

3.1.4. XPS study of oxygen mobility and the chemical state of the elements. X-ray photoelectron spectroscopy (XPS) analysis was carried out to investigate the surface chemical state of the samples. Survey spectra (Fig. S2†) comprise the lines of O, Ce, Zr, C and Cu (for modified samples). Some authors[37,38] believe that the presence of carbon promotes the formation of active oxygen species, such as superoxide (O_2^-), *via* oxygen adsorption on the reduced surface of ceria near carbon species:

$$Ce^{3+}–V_O + O_2 \rightarrow Ce^{4+}–(O_2^-),$$

where V_O is an oxygen vacancy.

Thus, ceria/soot contact, or ceria/surface carbon contact in our case, may be the starting point of the active superoxide ion formation, which then reacts with carbon monoxide to form CO_2. However, additional amounts of CO_2 are formed due to soot oxidation at higher temperatures (starting from 350 °C), leading to an overestimation of CO conversion in this range.

Br (0.5–1.1 at%) and K (0.2–0.4 at%) XPS lines are observed in the survey spectra of the CTAB- and SD-templated samples, correspondingly, consistent with the SEM-EDS results.

At first glance, the influence of residual bromine on the catalytic activity of the CTAB-templated samples is possible. However, similar Ni–$Ce_{1-x}Zr_xO_2$ samples produced by co-precipitation of precursor salts with ammonium bromide or KOH demonstrated nearly the same catalytic properties in dry reforming of methane.[39] On the basis of this result the effect of residual bromine species can be excluded.

High resolution Ce 3d XPS spectra are presented in Fig. 4a. In these complex spectra, the intense pronounced line at E_B = 916 eV testifies that the predominant oxidation state of Ce in all samples is Ce^{4+}. However, the presence of a Ce^{3+} fraction cannot be excluded. To discover the Ce^{3+}/Ce^{4+} ratio the intensity of the line at E_B = 916 eV was calculated relative to the integral intensity of the Ce 3d region, and compared with that for the reference CeO_2 spectrum. The results are shown in Table 1. The highest Ce^{3+}/Ce^{4+} ratio was found in the non-modified CZ samples, while it is nearly the same for the CTAB- and SD-templated oxides and diminishes with the increase of calcination temperature.

Various reasons for the Ce^{3+} ion presence in CZ systems are discussed in the literature. The most probable reason is that oxygen vacancies on the surface should be balanced by the partial reduction of some Ce^{4+} ions to maintain general electroneutrality.[40] In addition, the presence of anionic Frenkel defects, in which some oxygen ions in a tetrahedral arrangement migrate to octahedral voids forming vacancies, was demonstrated using neutron diffraction for fluorite-type crystal structures,[41] *e.g.* ceria. Incorporation of Zr^{4+} into the CeO_2 lattice also leads to an increase of the Ce^{3+} fraction in the material.[40,42]

According to the above mentioned reasons, it can be expected that CZ double oxide systems calcined at 500 °C and containing more Ce^{3+} will be more active in CO oxidation than their counterparts calcined at 600 °C, regardless of the template type.

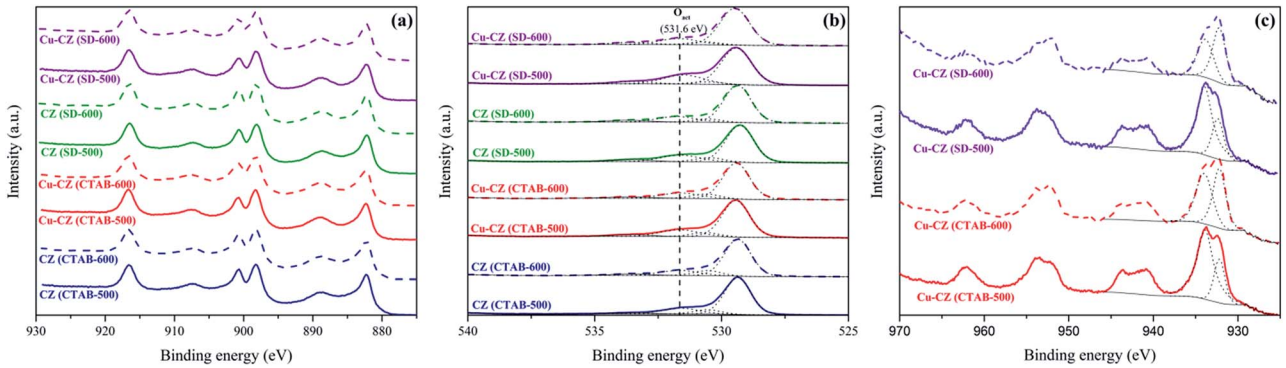

Fig. 4 Ce 3d (a), O 1s (b) and Cu 2p (c) high resolution XPS spectra of the studied samples.

An important trend observed for both types of system is that modification with CuO leads to a significant decrease of the Ce^{3+} fraction in all samples, down to zero for the Cu–CZ (CTAB-500) sample. This trend is explained by the electron transfer between Cu^{2+} and Ce^{3+} ions according to the following redox equation:

$$Cu^{2+} + Ce^{3+} \leftrightarrow Cu^{+} + Ce^{4+}$$

Such a process may be intrinsic to the mixed Cu–Ce oxide phase, so this fact confirms the hypothesis about partial incorporation of Cu into the CZ lattice, proposed to explain the decrease of the crystal lattice parameter *a*.

However, the ability of Ce^{4+} to fast partial reduction under XPS conditions was demonstrated in the literature.[43] This fact forces us to treat the XPS data on the Ce^{3+}/Ce^{4+} ratios very cautiously.

The high resolution O 1s XPS spectra of all samples presented in Fig. 4b contain a main peak with a pronounced shoulder at the high energy side. These spectra were fitted by four components. Less intensive components at 530.6 and 533.6 eV are possibly due to the oxygen in the carbon-containing surface groups, namely C–O and CO_3^{2-}, or in OH^-.[44] A relatively high surface carbon content found by EDS and XPS confirms this assumption.

The most intensive O 1s component at 529.6 eV corresponds to the lattice oxygen surrounded by Ce^{4+} ions.[45] The component at 531.6 eV can be associated with the presence of oxygen vacancies[46] or the active surface oxygen in several forms: (1) low coordinated highly polarized oxide ions on the surface of nanocrystals;[47] (2) adsorbed or weakly bound surface oxygen as a peroxide or superoxide centers which are formed on the surface during stepwise incorporation of gas phase oxygen into an oxide lattice.[48] The calculated fraction of this component (O_{act}, %) is presented in Table 1. This value is obviously higher for the SD-templated sample than for the corresponding CTAB-templated one. Therefore, despite a nearly equal Ce^{3+}/Ce^{4+} ratio in the biomorphic and CTAB-templated samples, the former contains more active oxygen, and can demonstrate higher activity in CO oxidation. This is especially true for the samples calcined at 500 °C, where the fraction of O_{act} is the most significant. The highest O_{act} content is observed for Cu–CZ (SD-500).

High resolution Cu 2p XPS spectra (Fig. 4c) prove the presence of Cu^+ ions (~932.2 eV) in addition to the predominating Cu^{2+} ions (~934 eV). It should be noted that the results of the quantitative estimation of the Cu^+ fraction need to be treated carefully, because partial reduction of Cu^{2+} to Cu^+ in XPS experimental conditions was observed earlier.[49] Nevertheless, comparing the acquisition time of XPS analysis and the rate of Cu^{2+} reduction, the presence of Cu^+ is believed to be well-established.

The calculated Cu^+/Cu^{2+} ratios are presented in Table 1. It is clearly seen that the increase of calcination temperature causes the growth of the Cu^+ fraction. In ref. 50 the same effect was found by XPS for Cu–Ce–O composite catalysts prepared by co-precipitation, while the fraction of isolated Cu^{2+} ions decreased. STEM/EDS analyses demonstrate the migration of copper from the bulk to the surface of these composites, causing the formation of copper clusters strongly interacting with cerium oxide. Such an interaction contributes to the reduction of Cu^{2+}. Other authors believe that Cu^+ appears due to metal ion transfer between CuO and CeO_2 on the phase boundary, caused by the similarity of the ionic radii of Ce^{4+} and Cu^+.[51] Cu^+ is known to be an active adsorption center for CO, and therefore can strongly influence the catalytic properties of ceria or double CZ oxides in CO oxidation.[50]

XPS data also demonstrate that the oxygen vacancy concentration in biomorphic samples is higher that it could be expected on the basis of Ce^{3+} fraction estimation. The possible reason is the intercalation of K and Ca ions into the CZ crystal lattice.

3.1.5. Temperature-programmed reduction study of the redox properties. The redox properties of the samples were investigated using TPR with H_2 (Fig. 5a and b). For all samples the TPR profiles were divided into three temperature ranges according to the nature of the hydrogen consumption peaks. H_2 consumptions calculated for the whole TPR profile and for separate temperature ranges, marked by dashed lines in Fig. 5, are shown in Table 2. To consider the different amounts of Cu and Ce in the samples and to allow comparison of CZ with the Cu-modified samples, H_2 uptakes were normalized to the Ce content.

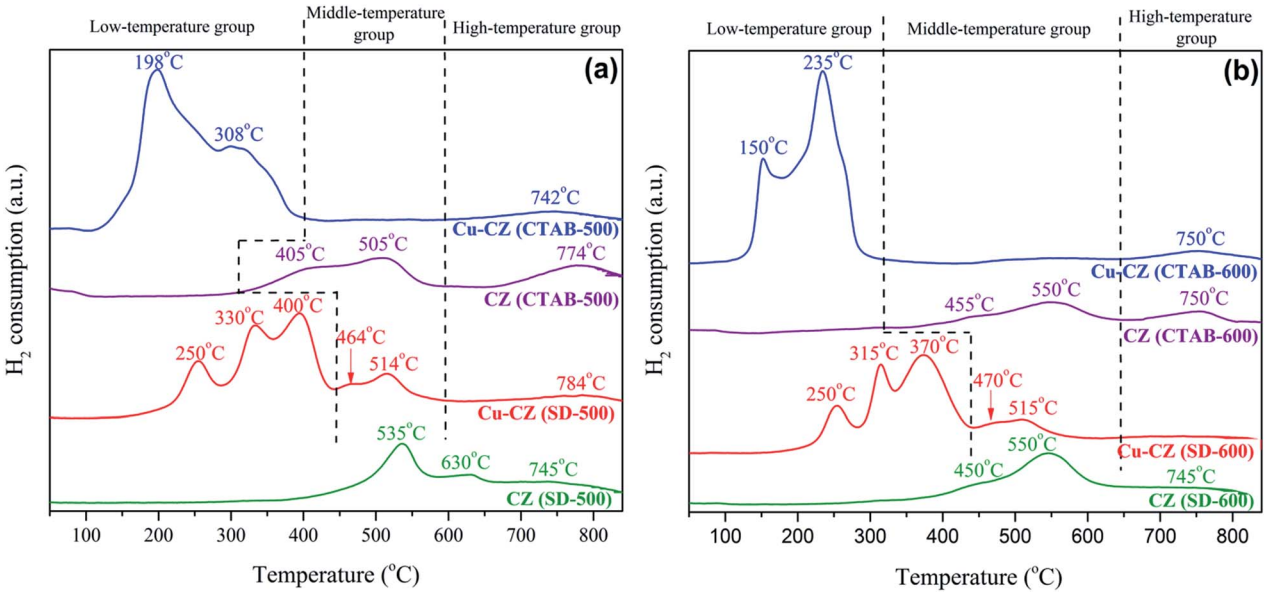

Fig. 5 H_2-TPR profiles of CZ and Cu–CZ, calcined at 500 °C (a) and 600 °C (b).

Firstly, we will consider the TPR profiles of the CZ samples. It is known that Zr^{4+} is not reducible up to 1000 °C.[52] The profiles of the CZ (CTAB-500) and CZ (SD-500) samples look similar to those of CZ (CTAB-600) and CZ (SD-600). They comprise three broad peaks with maxima around 450, 550 and 750 °C, which can be attributed to the reduction of CeO_2 on the surface, in the subsurface layer and in the bulk.[11,53,54] The maxima of the two peaks in the middle-temperature region in the TPR profile of CZ (CTAB-500) are shifted to lower temperature. Therefore, the reduction of Ce^{4+} proceeds easier in the surface and subsurface layers of this sample.

The ratio of hydrogen uptake at 450–550 °C (middle-temperature range) and at around 750 °C (high-temperature range) is higher for CZ (CTAB-600) than for CZ (CTAB-500) (1.8 and 1.4, respectively). It seems that due to structure ordering which is observed as a significant decrease of S_{BET} the reduction of surface and especially bulk ceria in CZ (CTAB-600) is hindered. This guess is confirmed by the decrease in the total H_2 uptake for both types of CZ sample calcined at higher temperature (Table 2).

Two peaks in the middle-temperature range of the TPR profile of CZ (SD-500) are significantly shifted to higher temperatures in comparison with CZ (SD-600). This can be explained by the decrease of S_{BET} which hinders both the contact of H_2 with the surface and as a result the removal of H_2O formed during reduction. H_2 uptake for both SD-templated samples is higher than that for the corresponding CTAB-templated ones, and increases remarkably in the case of CZ calcined at 500 °C (Table 2). Therefore, CZ (SD-500) is integrally more reducible than CZ (SD-600), but the reduction of surface and subsurface species proceeds more easily in CZ (SD-600). CZ (SD-600) is expected to catalyze CO oxidation at lower temperatures than CZ (SD-500).

To summarize, the transition from the organic template to the biotemplate and the decrease of calcination temperature allow an increase in the total H_2 consumption by the CZ samples

Table 2 H_2 consumption during TPR investigation from 30 to 850 °C

	H_2 consumption, μmol $[g(Ce)]^{-1}$				
Sample	Low-temperature range	Cu^{2+} reduction[a]	Middle-temperature range	High-temperature range	Total
CZ (CTAB-500)	N/A[b]	N/A	1307	954	2261
CZ (CTAB-600)	N/A	N/A	1290	703	1993
Cu–CZ (CTAB-500)	4003	2908	N/A	762	4765
Cu–CZ (CTAB-600)	3874	1920	N/A	764	4638
CZ (SD-500)	N/A	N/A	N/A	N/A	2467
CZ (SD-600)	N/A	N/A	N/A	N/A	2290
Cu–CZ (SD-500)	2755	2081	1068	1121	4944
Cu–CZ (SD-600)	2900	1977	962	1071	4933

[a] Calculated value for the reduction of the amount of copper determined in the sample by AAS, providing that the sample contains only Cu^{2+}. [b] N/A means that the group of peaks is absent or difficult to separate.

(Table 2) that can be explained by the increase of active oxygen content on the surface. This fact is confirmed by XPS data.

TPR profiles of both CTAB-templated Cu–CZ samples comprise the peak of bulk Ce^{4+} reduction with a maximum at approx. 750 °C, and a group of low-temperature peaks, which is usually attributed to copper reduction, whereas no peaks are observed around 500–550 °C. Earlier it was found that the addition of Cu completely changes the reduction behavior of CeO_2.[55] The reduction of surface ceria promoted by copper is observed at lower temperatures. If the same is true for CTAB-templated samples, the hydrogen consumption in the low-temperature range will be higher than that expected as a result of only copper reduction.

In addition to the total hydrogen uptake for Cu-containing samples, Table 2 shows the amount of H_2 that corresponds to the complete reduction of copper, the content of which was found by AAS, providing that it is in the fully oxidized state of Cu^{2+}. The excessive H_2 uptake is observed at 30–450 °C (low-temperature range) for both CTAB-templated Cu-containing catalysts (1095 and 1954 μmol $[g(Ce)]^{-1}$ for Cu–CZ (CTAB-500) and Cu–CZ (CTAB-600), respectively). These values are comparable with the H_2 uptake at middle temperatures (peaks around 500–550 °C) by the corresponding double oxides CZ (CTAB-500) and CZ (CTAB-600) (1307 and 1290 μmol $[g(Ce)]^{-1}$, respectively), attributed above to the reduction of Ce^{4+} in the surface and subsurface layers (the corresponding peaks are absent in the profiles of Cu-containing CTAB-templated samples). Such changes can be caused by the formation of double or triple Cu-containing surface oxides $Cu_yCe_xZr_{1-x-y}O_{2-z}$ or $Cu_yCe_xO_{2-z}$. Besides, as it was noted in ref. 53, independent of the preparation method, some copper dissolution in the CZ phase takes place providing the formation of highly dispersed copper ions that promote surface ceria reduction at lower temperatures. Note that for Cu–CZ (CTAB-600) the excessive H_2 uptake in the low-temperature range is higher than the total H_2 consumption during TPR of the corresponding CZ (CTAB-600) sample. This difference can be explained both by the variation in the valence state of Ce in these samples and by hydrogen spillover from copper species to the CZ support. Fundamentally, these results confirm the possibility of cerium reduction at unusually low temperatures in the presence of copper oxides.

The low-temperature group of peaks is broader for Cu–CZ (CTAB-500) (130–420 °C) than for Cu–CZ (CTAB-600) (130–320 °C). So, the reduction of bulk components, typically proceeding at higher temperatures (320–420 °C), is hindered for the sample calcined at 600 °C due to structure ordering, as it was found for corresponding CZ samples.

The TPR profiles of Cu–CZ (SD-600) and Cu–CZ (SD-500) are similar. They comprise broad low intense peak of bulk cerium reduction at about 780 °C, two peaks of surface and subsurface cerium reduction at about 460–515 °C, and a low-temperature group of three peaks at 250–400 °C. The peaks of surface and subsurface cerium reduction at about 464 and 514 °C for Cu–CZ (SD-600) nearly coincide with that for CZ (SD-600), however hydrogen uptake in this temperature range is lower for the Cu-modified sample. It can be proposed that the fraction of cerium is reduced at lower temperatures, as in the case of the CTAB-templated Cu-containing samples.

For Cu–CZ (SD-500) the discussed peaks of surface and subsurface cerium reduction are observed at the same temperatures (464 and 514 °C) as for Cu–CZ (SD-600); they are shifted to lower temperatures in comparison with the CZ (SD-500) profile. Note that the S_{BET} of Cu-CZ (SD-500) is unusually high ($93 \pm 9\ m^2\ g^{-1}$) for the SD-templated sample, and is similar to that of Cu–CZ (CTAB-500), not of CZ (SD-500). The availability of the surface to H_2 due to structure disordering provides easier reduction of surface and subsurface cerium in Cu-CZ (SD-500).

The group of low-temperature peaks is shifted to higher temperatures for the Cu-modified SD-templated samples in comparison with the CTAB-templated ones. According to the discussion above, this group of peaks can comprise up to six components, corresponding to the reduction of Cu^{2+} to Cu^+, Cu^+ to Cu^0, and Ce^{4+} to Ce^{3+} in the bulk and on the surface. The position of these peaks may shift depending on the material surrounding copper and cerium. For instance, it could be expected that the reduction of CuO in close vicinity to CZ or $Cu_yCe_xZr_{1-x-y}O_{2-z}$ will proceed in a different temperature range. The exact attribution of all components is a very difficult task, but many considerations can be found in the literature. Thus, the intensive signal at 198 °C can be ascribed to the reduction of CuO species strongly interacting with the CZ support,[56,57] to the partial reduction of surface Ce^{4+} to Ce^{3+}, and to the total reduction of dispersed Cu_2O particles to Cu.[58] The shoulder at higher temperatures shows the reduction of large CuO particles which are not associated with the support,[56,57,59] or the reduction of Ce^{4+} to Ce^{3+} and Cu^+ to Cu^0 in the bulk of the catalyst.[58] Similar attribution of this higher-temperature component was proposed to describe the TPR profile of CuO/CeO_2.[60] The peaks at 250 and 330 °C can arise due to hydrogen consumption by weakly bonded O^{2-} ions in surface oxygen vacancies of CuO, and by interphase O^{2-} ions nearby oxygen vacancies, respectively.[59]

Therefore, the TPR results demonstrate the significant difference in the Cu state for the CTAB-templated and biomorphic catalysts. The Cu–CZ (CTAB-500) sample shows much more in common with samples reported early in the literature, whereas reduction of Cu species in Cu–CZ (SD-500) proceeds at a higher temperature. The probability of double Cu–Ce or triple Cu–Ce–Zr oxide surface phase formation is higher in CTAB-templated systems, demonstrating a more close interaction of Ce with Cu in the surface and subsurface layer. The total H_2 consumption increases as a result of CZ modification with Cu; it is higher for SD-templated samples than for the corresponding CTAB-templated ones. The decrease of calcination temperature increases H_2 uptake for Cu-containing CTAB-templated samples, and has no influence on SD-templated ones.

The presence of various Cu species in SD-samples results in the broad temperature range of copper reduction (200–400 °C) which may enhance the catalytic properties in CO oxidation.

3.2. Catalytic activity in CO oxidation

Carbon monoxide is formed in various industrial processes and during fuel burning in engines.[24] It is one of the main air

pollutants, and can cause mortal poisoning. CO is a colorless and odorless gas, therefore its presence in air is difficult to detect. Catalytic total oxidation is the most effective way to avoid toxic CO emissions.

The catalytic efficiency of the samples was estimated on the basis of CO conversion to CO_2 in the temperature range from 100 to 400 °C. The results are presented as steady-state CO conversion *vs.* temperature curves (Fig. 6). All tested samples were active in CO oxidation, but the temperature ranges of their catalytic action were significantly different.

3.2.1. The influence of calcination temperature and Cu modification on the catalytic properties of CTAB-templated samples. The decrease of the calcination temperature of double oxides from 600 to 500 °C (Fig. 6a) leads to an improvement of CO conversion at high temperatures (350–400 °C), possibly due to the higher Ce^{3+}/Ce^{4+} ratio in CZ (CTAB-500) in comparison with CZ (CTAB-600). For illustration purposes graphs of CO conversion *vs.* reaction temperature are shown separately for the CTAB- and SD-templated samples in Fig. S3a and b,† respectively.

According to the literature,[61] the increase of the Ce^{3+}/Ce^{4+} ratio leads to the increase of the amount of oxygen vacancies and unsaturated chemical bonds on the surface of a catalyst, and to the growth of the surface content of active oxygen. Lattice oxygen mobility is governed by the energy of oxygen vacancy formation and by the activation energy of oxygen migration in the lattice, and therefore significantly increases with temperature. Possibly due to this reason, CO conversion at a lower temperature (150–300 °C) doesn't depend on the calcination temperature.

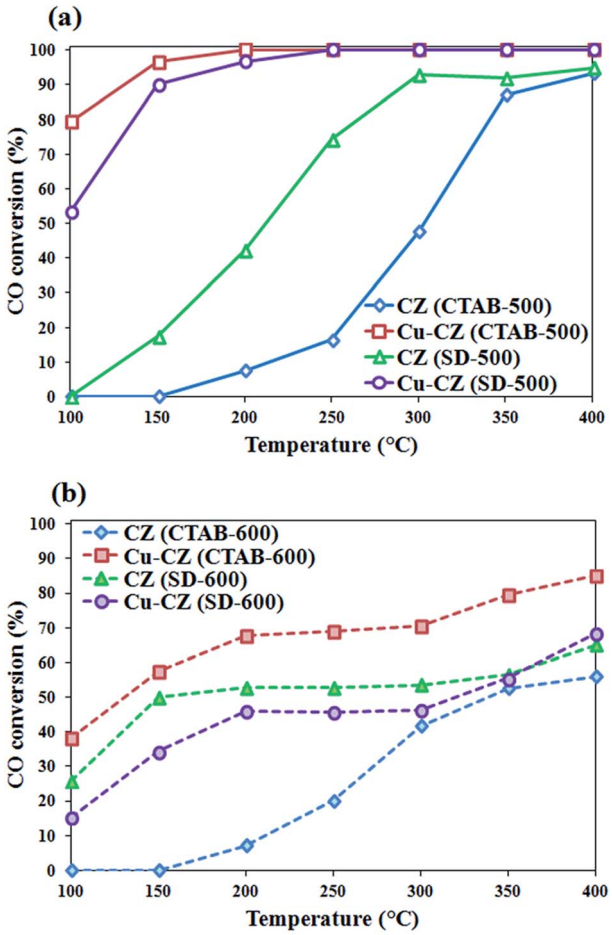

Fig. 6 CO conversion *vs.* reaction temperature for the samples calcined at 500 °C (a) and 600 °C (b).

Comparing the pairs of CZ (CTAB) and Cu–CZ (CTAB) samples, calcined at the same temperature (Fig. 6a and b and S3a†), it is evident that CuO addition significantly improves the catalytic efficiency in the whole temperature range and widens the range of high CO conversion to low-temperature region in both cases. In the Cu-modified system the Ce^{3+} content is lower and O_{act} content is comparable with that in CZ (CTAB). Therefore, the improvements are possibly connected not only with the presence of bulk CuO, but also with the partial incorporation of Cu into the CZ lattice, the evidence of which for Cu–CZ (CTAB-500) was found by XRD, and with the formation of double and triple Cu–Ce and Cu–Ce–Zr oxide surface phases, which was proposed on the basis of TPR data. Recent investigations have shown[36] that CO oxidation is directly catalyzed by dispersed copper ions in the mixed oxide phase. Therefore, the formation of the mixed $Cu_yCe_xO_{2-z}$ or $Cu_yCe_xZr_{1-x-y}O_{2-z}$ phases in the bulk or on the surface of CZ will favor the catalytic activity of the Cu–CZ systems.

Despite lower O_{act} content, Cu–CZ (CTAB-500) provides significant improvement of CO conversion in comparison with Cu-CZ (CTAB-600). This can be explained by the higher CuO loading found by AAS (Table 1) (29.0 in Cu–CZ (CTAB-500) against 21.2 mol% in Cu–CZ (CTAB-600)) and higher S_{BET}.

A strong influence of S_{BET} on the catalytic performance is observed for CZ (CTAB-500). This sample shows the most developed surface ($S_{BET} = 165\ m^2\ g^{-1}$), and provides better CO conversion at 350–400 °C, compared to modified Cu–CZ (CTAB-600) with much lower S_{BET} ($62\ m^2\ g^{-1}$). The content of O_{act} in these samples is high (see Table 1), but the Ce^{3+} content in CZ (CTAB-500) is the highest among all the samples, providing many oxygen vacancies. The agglomerates of CuO in Cu–CZ (CTAB-600) possibly partially block the access of the CO molecules to the CZ surface making this sample less effective than CZ (CTAB-500) at high temperatures, at which high oxygen mobility in CZ plays a crucial role.

3.2.2. The influence of calcination temperature and CuO modification on the catalytic properties of biomorphic samples. The plot of CO conversion to CO_2 *vs.* temperature for the biomorphic systems is presented in Fig. 6 and S3b.†

An interesting effect was found for the double CZ systems: at low temperature CZ (SD-600) provides higher CO conversion than CZ (SD-500), but starting from 250 °C the inverse relation is observed. An improved efficiency of CZ (SD-500) at higher temperatures can be caused by the higher content of oxygen vacancies, which is confirmed by the significant content of O_{act} and Ce^{3+} (17.1% and 0.14% CZ (SD-500) *vs.* 15.1% and 0.09% for CZ (SD-600)) estimated by XPS (Table 1). The difference in CO conversion at low temperature can be attributed to the changes in the extent of the ash admixture (Ca and K) interaction with the CZ lattice. At a high calcination temperature (600 °C) Ca and

K ions more effectively penetrate the crystal lattice of CZ than at 500 °C, which increases the electron deficiency of this lattice and improves lattice oxygen mobility, even at lower Ce^{3+} content.

Modification of CZ by CuO leads to the improvement of the catalytic action of the biomorphic systems, calcined at 500 °C, in the whole studied temperature range. It is consistent with the increase of O_{act} content, decrease of lattice parameter, and significant improvement of S_{BET} of Cu–CZ (SD-500) (Table 1).

In contrast, Cu–CZ (SD-600) is somewhat less effective than CZ (SD-600). In this case S_{BET}, the lattice parameter and the O_{act} content are nearly the same for both samples. In addition, CO conversion on these samples in the range of 200–350 °C is limited by 53–56% (Fig. 6 and S3b†). Such a saturation of the CO conversion *vs.* temperature curves is also observed for CZ (CTAB-600) (about 55% conversion). This may be connected with the use of a stoichiometric CO : O_2 mixture if the reaction proceeds predominantly *via* the Mars–van Krevelen mechanism on the catalyst with high lattice oxygen mobility. At high temperature, the amount of O_2 in the reaction mixture is not enough to compensate for the lattice oxygen spent for CO oxidation.

3.2.3. Comparison of biomorphic and CTAB-templated systems. The non-modified CZ (SD) samples in comparison with CZ (CTAB) provide higher CO conversion in nearly the whole temperature range (150–300 °C) independent of calcination temperature. A similar result was described in our previous work for CZ systems prepared using CTAB or SD templates and calcined at 630 °C and 600 °C respectively.[24] On the basis of XRD and Raman spectroscopy data, better performance of SD-templated CZ was explained by the improved oxygen mobility in the biomorphic systems, which can be caused by the presence of ash impurities inherited from the sawdust template.

As it was shown above by EDS and XPS, all biomorphic samples contain Ca and K. The intercalation of the K and Ca ions into the CZ oxide lattice is the possible reason for the significant increase of the active oxygen O_{act} fraction in the biomorphic samples as compared to the CTAB-templated ones, which is clearly seen from the XPS data (Table 1).

It was noted in the literature that the introduction of a small amount of CaO to CeO_2 (in atomic ratios Ca/Ce = 0.1)[14] or to double CZ systems[15] promotes the formation of oxygen vacancies, leading to the improvement of the catalytic activity in CO oxidation.

The positive action of moderate amounts (below 20 mol%) of bulky cations, *e.g.* Ca^{2+}, on the number of anionic vacancies and oxygen mobility due to a distortion of the fluorite lattice of the CZ oxide was shown in ref. 16 and 17. According to these studies the presence of Ca admixture can lead to an increase of CO conversion. Improvement of the catalytic action of CZ in CO oxidation by the deliberate addition of Ca and K to CZ during co-precipitation with a subsequent calcination at 500 °C was also observed in our previous study.[13] The facilitation of the formation of strongly nucleophilic peroxide and superoxide complexes upon the chemisorption of oxygen on CZ oxides confirmed by XPS and TPR data was proposed in this study as the most probable reason for the promotion effect of potassium. The stabilization of superoxide and peroxide species in the presence of alkali ions was demonstrated early.[62]

Addition of CuO to both biomorphic and CTAB-templated CZ systems calcined at 500 °C (Fig. 6a) improves CO conversion in all temperature ranges studied in this work primarily due to the inclusion of a new redox pair of Cu^+/Cu^{2+} into the catalytic cycle and the formation of mixed $Cu_yCe_xO_{2-z}$ or $Cu_yCe_xZr_{1-x-y}O_{2-z}$ phases. The other reasons for the improvement of CO conversion are the decrease of crystallinity and the increase of surface inhomogeneity in comparison with the systems calcined at 600 °C.

On the basis of the literature data,[63] the support of CuO on CeO_2-containing systems can provide (depending on a temperature range of CO oxidation) both the additional adsorption sites and/or an additional redox pair of Cu^+/Cu^{2+}, according to the following scheme:

$$(Cu^{n+})_{surf} + CO \rightarrow (Cu^{n+})_{surf}\text{–}CO_{ads} \quad (1)$$

$$2(Cu^{n+})_{surf} + O_2 \rightarrow 2(Cu^{n+})_{surf}\text{–}O_{ads} \quad (2)$$

$$(Cu^{n+})_{surf}\text{–}CO_{ads} + (Cu^{n+})_{surf}\text{–}O_{ads} \rightarrow 2(Cu^{n+})_{surf} + CO_2 \quad (3)$$

$$(Ce^{4+}/Cu^{2+}\text{–}O^{2-})_{surf} + CO \rightarrow (Ce^{3+}/Cu^{+}\text{–}V_O)_{surf} + CO_2 \quad (4)$$

$$(Ce^{3+}/Cu^{+}\text{–}V_O)_{surf} + CO \rightarrow (Ce^{3+}/Cu^{+}\text{–}V_O)_{surf}\text{–}CO_{ads} \quad (5)$$

$$(Ce^{3+}/Cu^{+}\text{–}V_O)_{surf}\text{–}CO_{ads} + O_2 \rightarrow (Ce^{4+}/Cu^{+}\text{–}O_2^{-})_{surf}\text{–}CO_{ads} \quad (6)$$

$$(Ce^{3+}/Cu^{+}\text{–}V_O)_{surf}\text{–}CO_{ads} + O_2 \rightarrow (Ce^{4+}/Cu^{2+}\text{–}O_2^{2-})_{surf} + CO_2 \quad (7)$$

$$(Ce^{4+}/Cu^{2+}\text{–}O_2^{2-})_{surf} + (Ce^{3+}/Cu^{+}\text{–}V_O)_{surf}\text{–}CO_{ads} \rightarrow (Ce^{4+}/Cu^{2+}\text{–}O^{2-})_{surf} + CO \quad (8)$$

Eqn (1)–(3) describe the Langmuir–Hinshelwood mechanism of CO oxidation at relatively low reaction temperatures, when the oxygen mobility is hindered. In this mechanism, Cu^{2+} or Cu^+ on the surface of CuO, Cu_2O, $Cu_yCe_xO_{2-z}$ or $Cu_yCe_xZr_{1-x-y}O_{2-z}$ serve as active sites.

At higher temperatures, the lattice oxygen mobility grows and the kinetic scheme of Mars–van Krevelen (reactions (4)–(8)) becomes predominant. The joint action of the redox pairs of Cu^+/Cu^{2+} and Ce^{3+}/Ce^{4+} has been described by many authors.[22,62,63] The reaction mechanism comprises CO oxidation by surface oxygen species (O^{2-}) followed by the formation of CO_2 and oxygen vacancies (V_O) accompanied by the reduction of a Ce^{4+}/Cu^{2+} pair (reaction (4)).[63,64] Then CO adsorbs an oxygen vacancy and reacts with O_2 to form superoxide (O_2^-) and peroxide (O_2^{2-}) species (reactions (6) and (7)), which are stabilized due to the promoting action of the alkali metal ions. At the final stage, the initial active site structure is recovered by reaction (8).

However, Cu modification deteriorates the catalytic efficiency of the biomorphic CZ sample calcined at 600 °C. It is possible that in this case the CuO phase blocks the active sites situated on the surface of CZ, which provides good oxygen mobility due to the lattice inclusion of Ca^{2+} and K^+.

Cu–CZ (CTAB-500) is somewhat more active than Cu–CZ (SD-500) at 100–150 °C, mainly due to the significantly higher CuO content, and in some extent due to the stronger CuO interaction with the CZ support in the CTAB-templated system, found by TPR. However, the difference between these samples is not so prominent, if the whole temperature range is considered, considering that the S_{BET} values for these samples are comparable. Note that on the basis of TPR data we can expect worse catalytic activity of the Cu-modified biomorphic sample, due to the weaker interaction of CuO with CZ. But it seems that the promoting action of Ca and K ions on CZ is the most important factor contributing to the improvement of the catalytic properties of Cu–CZ (SD-500). At equal CuO loading the biomorphic catalyst will probably be a good competitor to the CTAB-templated counterpart.

The results of this study confirm that sawdust, which is an industrial waste, can be effectively used instead of organic templates for the preparation of CO oxidation catalysts on the basis of ceria and zirconia. However, for the development of industrial methods the problem of the reproducibility of the catalytic properties should be addressed. Sawdust of various wood species, grown in different geographical locations, has a similar main chemical composition, but a variable content of ash impurities and other components. Considering the strong dependence of the catalytic properties on the presence of ash impurities, to provide reproducibility of the catalytic results the content of the admixture of alkali or alkaline-earth metal salts can be adjusted by mixing different sawdust batches or by the intentional addition of the desired components. Reaching an optimal method of catalyst preparation from sawdust requires the knowledge of the influence of the content of admixture on the catalytic properties, which will be the focus of the future work.

4. Conclusions

CZ and Cu–CZ oxide systems, prepared by biotemplate (wood sawdust, SD) impregnation with metal salts and subsequent calcination at 500 or 600 °C, demonstrate high efficiency in CO oxidation to CO_2 at 100–400 °C. Calcination at lower temperatures provides more effective catalysts, independent of the presence of Cu. Calcination at 600 °C leads to a decrease in the Ce^{3+} : Ce^{4+} ratio and excessive ordering of the crystal structure, which is confirmed by XRD data and by the decrease of the specific surface area. As a result, improved oxygen mobility and better contact of CO with the surface of the catalyst are achieved in the catalysts calcined at 500 °C.

The double oxide biomorphic sample CZ (SD-500) is much more effective in CO oxidation in comparison with the similar CTAB-templated sample CZ (CTAB-500) despite a two times less S_{BET} value. Possible reasons for such an improvement are (1) the presence of Ca and K additives inherited from wood sawdust, and (2) the modification of the phase composition, found by XRD. Such a modification may result from the intercalation of potassium and/or calcium ions into the crystal lattice and lead to the change in lattice oxygen mobility in the mixed oxide phases. This change in oxygen mobility affects the Ce^{3+} : Ce^{4+} ratio and provides an improvement of the high-temperature efficiency in CO oxidation through the Mars–van Krevelen mechanism. In addition, alkali metal ions stabilize strongly nucleophilic peroxide and superoxide complexes on the catalytic surface. These complexes can participate in CO oxidation.

Modification with Cu is very efficient for the biomorphic as well as the comparative CTAB-templated CZ systems calcined at 500 °C. Biomorphic sample Cu–CZ (SD-500) is a bit less active than Cu–CZ (CTAB-500) only at 100 and 150 °C, primarily due the decreased CuO content, and the difference in CuO interaction with the CZ support, found by TPR. At higher temperatures both samples show the same CO conversion close to 100%. The XRD, XPS and TPR data testify that Cu in modified systems exists as a separate CuO phase, in small amount as Cu^+, and partially is incorporated in surface $Cu_yCe_xZr_{1-x-y}O_{2-z}$ and/or $Cu_yCe_{1-y}O_{2-x}$ phases. The formation of Cu-containing double or triple oxide surface phases is less typical for biomorphic than for CTAB-templated samples. According to the TPR data the peaks of the surface and subsurface Ce reduction move to a lower temperature group characteristic for Cu reduction. It seems that CuO provides low-temperature CO oxidation through the Langmuir–Hinshelwood mechanism; a Cu^+/Cu^{2+} pair can also participate as an additional redox pair in high-temperature CO oxidation by the Mars–van Krevelen mechanism.

Modification with Cu of more ordered CZ (SD-600) leads to a decrease of CO conversion in the low temperature range of 100–250 °C, possibly due to the blocking of the active surface of CZ by CuO and the decrease of the accessible amount of the mobile lattice oxygen.

Therefore, the sawdust-templated samples calcined at 500 °C (CZ (SD-500) and Cu–CZ (SD-500)) showed very high efficiency in CO oxidation to CO_2, which was comparable (for Cu–CZ (SD-500)) or even better (for CZ (SD-500)) than that for their CTAB-templated counterparts. It seems that the decreased specific surface area of biomorphic CZ is compensated for by the promoting action of ash impurities and structure changes.

Conflicts of interest

There are no conflicts to declare.

Acknowledgements

This work was supported by the RF State Program for maintenance of leading scientific schools NSh-8845.2016.3 and in part by the Lomonosov Moscow State University Program of Development.

References

1 V. Singh and S. K. Chakarvarti, *American Journal of Bioengineering and Biotechnology*, 2016, **2**, 1–14.
2 C. R. Rambo and H. Sieber, *Adv. Mater.*, 2005, **17**, 1088–1091.
3 D. Yang, B. Du, Y. Yan, H. Li, D. Zhang and T. Fan, *ACS Appl. Mater. Interfaces*, 2014, **6**, 2377–2385.

4 C. Wang, L. Jing, M. Chen, Z. Meng, Z. Chen, F. Chen and W.-C. Oh, *J. Korean Ceram. Soc.*, 2017, **54**, 23–27.
5 A. N. Shigapov, G. W. Graham, R. W. McCabe and H. K. Plummer Jr, *Appl. Catal., A*, 2001, **210**, 287–300.
6 A. O. Turakulova, N. V. Zaletova, G. P. Murav'eva, M. V. Burova and V. V. Lunin, *Russ. J. Phys. Chem. A*, 2008, **82**, 1403–1406.
7 X. Li, T. Fan, Z. Liu, J. Ding, Q. Guo and D. Zhang, *J. Eur. Ceram. Soc.*, 2006, **26**, 3657–3664.
8 T. Montini, M. Melchionna, M. Monai and P. Fornasiero, *Chem. Rev.*, 2016, **116**, 5987–6041.
9 D. Duprez, C. Descorme, T. Birchem and E. Rohart, *Top. Catal.*, 2001, **16**, 49–56.
10 C. E. Hori, H. Permana, K. Y. S. Ng, A. Brenner, K. More, K. M. Rahmoeller and D. N. Belton, *Appl. Catal., B*, 1998, **16**, 105–117.
11 E. Aneggi, M. Boaro, C. de Leitenburg, G. Dolcetti and A. Trovarelli, *J. Alloys Compd.*, 2006, **408–412**, 1096–1102.
12 P. Fornasiero, R. Di Monti, G. Ranga Rao, J. Kaspar, S. Meriani, A. Trovarelli and M. Graziani, *J. Catal.*, 1995, **151**, 168–177.
13 I. Y. Kaplin, E. S. Lokteva, E. V. Golubina, K. I. Maslakov, S. A. Chernyak and V. V. Lunin, *Kinet. Catal.*, 2017, **58**, 585–592.
14 A. Iglesias-Juez, A. B. Hungría, O. Gálvez, A. Martínez-Arias, M. Fernández-García, A. Guerrero-Ruiz, J. C. Conesa and J. Soria, *Stud. Surf. Sci. Catal.*, 2001, **138**, 347–354.
15 M. Fernández-García, A. Martínez-Arias, A. Guerrero-Ruiz, J. C. Conesa and J. Soria, *J. Catal.*, 2002, **211**, 326–334.
16 T. Kuznetsova, V. Sadykov, L. Batuev, E. Moroz, E. Burgina, V. Rogov, V. Kriventsov and D. Kochubey, *J. Nat. Gas Chem.*, 2006, **15**, 149–163.
17 T. G. Kuznetsova, V. A. Sadykov, E. M. Moroz, S. N. Trukhan, E. A. Paukshtis, V. N. Kolomiichuk, E. B. Burgina, V. I. Zaikovskii, M. A. Fedotov, V. V. Lunin and E. Kemnitz, *Stud. Surf. Sci. Catal.*, 2002, **143**, 659–667.
18 E. Aneggi, C. de Leitenburg, G. Dolcetti and A. Trovarelli, *Catal. Today*, 2008, **136**, 3–10.
19 C. Telmo, J. Lousada and N. Moreira, *Bioresour. Technol.*, 2010, **101**, 3808–3815.
20 X. Zheng, X. Zhang, X. Wang, S. Wang and S. Wu, *Appl. Catal., A*, 2005, **295**, 142–149.
21 J.-L. Cao, Y. Wang, T.-Y. Zhang, S.-H. Wu and Z.-Y. Yuan, *Appl. Catal., B*, 2008, **78**, 120–128.
22 M. Moreno, L. Bergamini, G. T. Baronetti, M. a. Laborde and F. J. Mariño, *Int. J. Hydrogen Energy*, 2010, **35**, 5918–5924.
23 G. Avgouropoulos, T. Ioannides and H. Matralis, *Appl. Catal., B*, 2005, **56**, 87–93.
24 I. Y. Kaplin, E. S. Lokteva, E. V. Golubina, K. I. Maslakov, S. A. Chernyak, A. V. Levanov, N. E. Strokova and V. V. Lunin, *Russ. J. Phys. Chem. A*, 2016, **90**, 2157–2164.
25 X. B. Zhao, F. Chen, J. You, X. Z. Li, X. W. Lu and Z. G. Chen, *J. Mater. Sci.*, 2010, **45**, 3563–3568.
26 P. Scherrer, *Göttinger Nachrichten Math. Phys.*, 1918, **2**, 98–100.
27 A. Bryś, J. Bryś, E. Ostrowska-Ligęza, A. Kaleta, K. Górnicki, S. Głowacki and P. Koczoń, *J. Therm. Anal. Calorim.*, 2016, **126**, 27–35.
28 J. V. Bellini, R. Machado, M. R. Morelli and R. H. G. A. Kiminami, *Mater. Res.*, 2002, **5**, 453–457.
29 M. Aghayan, M. Gasik, I. Hussainova, F. Rubio-Marcos, L. Kollo and J. Kübarsepp, *Thermochim. Acta*, 2015, **602**, 43–48.
30 R. A. Lidin, L. L. Andreeva and V. A. Molochko, *Constants of inorganic substances*, Begell House, New York, 1995.
31 J. L. Cao, G. S. Shao, T. Y. Ma, Y. Wang, T. Z. Ren, S. H. Wu and Z. Y. Yuan, *J. Mater. Sci.*, 2009, **44**, 6717–6726.
32 H. Yen, Y. Seo, S. Kaliaguine and F. Kleitz, *Angew. Chem., Int. Ed.*, 2012, **51**, 12032–12035.
33 C. Ho, J. C. Yu, X. Wang, S. Lai and Y. Qiu, *J. Mater. Chem.*, 2005, **15**, 2193–2201.
34 P. Fornasiero, G. Balducci, R. Di Monte, J. Kašpar, V. Sergo, G. Gubitosa, A. Ferrero and M. Graziani, *J. Catal.*, 1996, **164**, 173–183.
35 Y. Liu, T. Hayakawa, K. Suzuki, S. Hamakawa, T. Tsunoda, T. Ishii and M. Kumagai, *Appl. Catal., A*, 2002, **223**, 137–145.
36 J. S. Elias, N. Artrith, M. Bugnet, L. Giordano, G. A. Botton, A. M. Kolpak and Y. Shao-Horn, *ACS Catal.*, 2016, **6**, 1675–1679.
37 E. Aneggi, D. Wiater, C. de Leitenburg, J. Llorca and A. Trovarelli, *ACS Catal.*, 2014, **4**, 172–181.
38 M. Machida, Y. Murata, K. Kishikawa, D. Zhang and K. Ikeue, *Chem. Mater.*, 2008, **20**, 4489–4494.
39 A. Wolfbeisser, O. Sophiphun, J. Bernardi, J. Wittayakun, K. Föttinger and G. Rupprechter, *Catal. Today*, 2016, **277**, 234–245.
40 D. Prusty, A. Pathak, M. Mukherjee, B. Mukherjee and A. Chowdhury, *Mater. Charact.*, 2015, **100**, 31–35.
41 E. Mamontov and T. Egami, *J. Phys. Chem. Solids*, 2000, **61**, 1345–1356.
42 G. Balducci, J. Kašpar, P. Fornasiero, M. Graziani, M. S. Islam and J. D. Gale, *J. Phys. Chem. B*, 1997, **101**, 1750–1753.
43 A. Galtayries, R. Sporken, J. Riga, G. Blanchard and R. Caudano, *J. Electron Spectrosc. Relat. Phenom.*, 1998, **88–91**, 951–956.
44 X. Y. Wang, Q. Kang and D. Li, *Catal. Commun.*, 2008, **9**, 2158–2162.
45 E. Nelson and K. H. Suhulz, *Appl. Surf. Sci.*, 2003, **210**, 206–221.
46 X. Tang, B. Zhang, Y. Li, Y. Xu, Q. Xin and W. Shen, *Catal. Today*, 2004, **93–95**, 191–198.
47 J. P. Holgado, G. Munuera, J. P. Espinós and A. R. González-Elipe, *Appl. Surf. Sci.*, 2000, **158**, 164–171.
48 D. Mukherjee, B. G. Rao and B. M. Reddy, *Appl. Catal., B*, 2016, **197**, 105–115.
49 M. C. Biesinger, L. W. M. Lau, A. R. Gerson and R. S. C. Smart, *Appl. Surf. Sci.*, 2010, **257**, 887–898.
50 W. Liu and M. Flytzani-Stephanopoulos, *J. Catal.*, 1995, **153**, 317–332.
51 S. Hocevar, U. O. Krasovec, B. Orel, A. S. Arico and H. Kim, *Appl. Catal., B*, 2000, **28**, 113–125.
52 I. Atribak, A. Bueno-López and A. García-García, *J. Catal.*, 2008, **259**, 123–132.

53 D. Terribile, A. Trovarelli, C. de Leitenburg, A. Primavera and G. Dolcetti, *Catal. Today*, 1999, **47**, 133–140.
54 W. Mista, M. A. Malecka and L. Kepinski, *Appl. Catal., A*, 2009, **368**, 71–78.
55 T. Caputo, L. Lisi, R. Pirone and G. Russo, *Appl. Catal., A*, 2008, **348**, 42–53.
56 W. Liu and M. Flytzani-Stephanopoulos, *Chem. Eng. J.*, 1996, **64**, 283–294.
57 L. Ma, M. F. Luo and S. Y. Chen, *Appl. Catal., A*, 2003, **242**, 151–159.
58 V. D. Araujo, J. D. A. Bellido, M. I. B. Bernardi, J. M. Assaf and E. M. Assaf, *Int. J. Hydrogen Energy*, 2012, **37**, 5498–5507.
59 J. L. Ayastuy, A. Gurbani, M. P. González-Marcos and M. A. Gutiérrez-Ortiz, *Int. J. Hydrogen Energy*, 2012, **37**, 1993–2006.
60 S. Sun, D. Mao, J. Yu, Z. Yang, G. Lu and Z. Ma, *Catal. Sci. Technol.*, 2015, **5**, 3166–3181.
61 Q.-F. Deng, T.-Z. Ren, B. Agula, Y. Liu and Z.-Y. Yuan, *J. Ind. Eng. Chem.*, 2014, **20**, 3303–3312.
62 P. Dolle, S. Drissi, M. Besançon and J. Jupille, *Surf. Sci.*, 1992, **269–270**, 687–690.
63 A. Martínez-Arias, M. Fernández-García, O. Gálvez, J. Coronado, J. Anderson, J. Conesa, J. Soria and G. Munuera, *J. Catal.*, 2000, **195**, 207–216.
64 Y.-Z. Chen, B.-J. Liaw and H.-C. Chen, *Int. J. Hydrogen Energy*, 2006, **31**, 427–435.